ChemElectroChem

Research Article
doi.org/10.1002/celc.202300283

Chemistry Europe
European Chemical Societies Publishing

www.chemelectrochem.org

N/P Co-doped Micro-/Mesoporous Carbons Derived from Polyvinyl Pyrrolidone–$Zn_{0.2}$@ZIF-67 with Tunable Metal Valence States towards Efficient Water Splitting

Yang Ming,[a] Yidi Wang,[a] Jiachuan Hua,[a] Chang Liu,[a] Jiashen Li,[c] and Bin Fei*[a, b]

The enhancement of electrocatalytic water splitting by modulating the intrinsic electronic environment of active sites has recently attracted lots of interest. Herein, cobalt-cobalt oxide (CoO_x) at carbons derived from metal-organic frameworks ($Zn_{0.2}$@ZIF-67) have been modulated by using post-phosphine (P-CoO_x/NCs), acid leaching (Co/NCs), and oxidation (O–CoO_x/NCs) treatments. With the assistance of polyvinyl pyrrolidone, the resultant carbons obtain a high surface area (645.7 $m^2 g^{-1}$) as well as a micro-/mesoporous system after carbonization at 920 °C. These advantages not only enhance the catalytic performance of catalysts, but also facilitate the charge transfer between interfaces towards the hydrogen evolution reaction (HER) and the oxygen evolution reaction (OER). As a result, the constructed water splitting cell fabricated with 900P-CoO_x/NCs requires a low overpotential (89 mV and 343 mV vs. reservable hydrogen electrode respectively) to drive HER and OER at 10 mA cm^{-2}, a low cell voltage (1.69 V), and a high stability with only 4.9% decay after 15 hours operation in the alkaline medium.

Introduction

Electrocatalytic water splitting to generate hydrogen and oxygen has attracted intensive attention as an effective solution to the global warming.[1,2] Among various candidates, transition metal-based materials derived from earth-abundant elements have been regarded as one of promising catalysts to boost the water splitting reaction. Nevertheless, strategies such as heteroatom doping,[3,4] defects engineering,[5,6] atom intercalation[7,8] and topographical control[9] were designed to significantly increase the number of accessible active sites and modulate the corresponding electronic environment of metallic atoms.

Zeolitic imidazolate frameworks (ZIFs) comprise these strategies by facile one-pot synthesis with ordered crystal structure, modular versatility such as tuneable atoms and organic linkers as well as low cost of synthesis.[10–12] Typically, cobalt element has been reported as a promising candidate due to the moderate adsorptive energy to the reaction intermediates according to density function theory calculations.[13] While the low intrinsic conductivity of ZIFs limits their applications as electrocatalysts. As a solution, high temperature carbonization is commonly employed to improve the intrinsic conductivity of ZIFs. Moreover, Co element will facilitate the graphitization of the frameworks by the formation of carbon nanotubes (CNTs) at high pyrolysis temperature[14–16] to enhance the conductivity of samples. Therefore, scientists have designed core-shell structure like ZIF-67@ZIF-8[17,18] to selectively functionalize the metallic Co located in carbons while Zn will evaporate at similar temperature (> 905 °C) to avoid the particles aggregations. However, under such harsh condition, the organic linkers will break down causing the collapse of whole framework due to the weak coordination force. This collapse hinders the available active sites in the inner part. To tackle this problem, protective/confinement pyrolysis has been proposed: for instance, ZIF-8 was mixed with surfactants such as polyvinylpyrrolidone (PVP)[19] or cetyltrimethylammonium bromide (CTAB)[20] to establish the cohesive interaction between interfaces. Or the construction of rigid interface such as pyrolyzing ZIF8@SiO_2[21] also achieved significant improvements in the maintenance of pore system and original surface area of ZIFs. As a result, the maintenance of pore systems or the construction of hierarchical structure can facilitate the electrolyte diffusion and mass transfer.

However, to best of our knowledge, few attentions have been paid to reveal the electronic modulation on the active sites of these protective carbonized samples from post treatment. As mentioned, most ZIFs carbonized at this harsh temperature will lose their original specific surface area, which finally lies in the range of S_{BET}~100–200 $m^2 g^{-1}$. The resultant

[a] Y. Ming, Dr. Y. Wang, Dr. J. Hua, Dr. C. Liu, Prof. B. Fei
School of Fashion & Textiles
The Hong Kong Polytechnic University
Hung Hom, Hong Kong, 999077 (China)
E-mail: bin.fei@polyu.edu.hk
Homepage: https://orcid.org/0000-0002-4274-1873

[b] Prof. B. Fei
Research Institute for Intelligent Wearable Systems
The Hong Kong Polytechnic University
Hung Hom, Hong Kong, 999077 (China)

[c] Dr. J. Li
Department of Materials
The University of Manchester
Manchester, M13 9PL (UK)

Supporting information for this article is available on the WWW under https://doi.org/10.1002/celc.202300283

products sluggish the overall catalytic performance due to the low possibility of active sites exposed to electrolyte. Moreover, instead of the forming CoP,[17,18,22] our studies confirm that the introduction of P element into the carbon frameworks from phosphine treatment can effectively influence the electronic environment of Co elements. As a result, the kinetics of overall water splitting reaction can be improved. In this study, we firstly manifested a high specific surface area (645.7 $m^2 g^{-1}$) and constructed a micro-mesoporous system of PVP assisted bimetallic ZIF-8/ZIF-67 (PVP-$Zn_{0.2}$@ZIF-67) at a pyrolysis temperature of 920 °C. Then we confirmed the introduction of P into the carbon frameworks by taking advantage of larger pores sizes to reveal optimized electronic state interaction. Moreover, we also investigated the effect among different Co valence states, where synergetic effect between Co^0 and Co^{2+} boosts the water reduction and Co^{2+} and Co^{3+} facilitate the water oxidation respectively. The as-synthesized catalysts were employed as bifunctional electrocatalysts towards hydrogen evolution reaction (HER) and oxygen evolution reaction (OER).

Results and Discussion

Morphology and Composition Characterization of CoOx/NCs

As illustrated in Figure 1a, the precursors are firstly prepared by incorporating cobalt ions into the ZIF-8 frameworks. A subsequent high temperature to evaporate Zn element, leave Co atoms interacting with O element in PVP agent. The obtained carbonized samples further experience the phosphine post treatments to modulate the electronic environment of cobalt atoms. The morphology of ZIF-8 and $Zn_{0.2}$@ZIF-67 nanoparticles were examined by TEM (Figure 1b–c). The resultant products show a well-constructed rhombic structure with an average size of 82 ± 15 nm.[17,23] Moreover, a lighter purple colour of $Zn_{0.2}$@ZIF-67 can be noticed due to the introduction of cobalt ions into ZIF-8 (Figure 1f), compared with that of pure ZIF 67, proving the efficient incorporation of Co^{2+} into ZIF-8 frameworks. After introduction of PVP, the morphology of PVP assisted $Zn_{0.2}$@ZIF-67 shows a distortion, which may originate from the incorporation of polymers into frameworks (Figure 1d).[24,25] Moreover, the PVP capping agent induces a larger particle size (up to 1 μm, Figure S1). From the X-ray diffraction pattern (XRD), it confirms the crystal structure of PVP assisted $Zn_{0.2}$/ZIF67 (Figure 1e). In consistent with the peaks of ZIF-8 s, when PVP and cobalt salts were introduced, those intensive peaks occurring at 7.3°, 10.4°, 12.7°, 14.7° and 17.9° are attributed to the (011), (002), (112), (022) and (222) facet, respectively.[17,26]

It is reported that the introduction of PVP polymer may induce the substitution of intercalated 2-MeIM, with slight distortion of ZIFs crystal structure.[25,27] Therefore, in this situation, PVP polymers are attached on ZIF surface, as well as incorporated into frameworks. After high temperature carbonization (920 °C) of PVP assisted $Zn_{0.2}$@ZIF-67, all crystal structures in ZIFs are destroyed where organic linkers denote to the nitrogen doped carbons (NCs). While for Zn element, it will vaporize at this temperature to prevent the aggregation of metallic particles,[28] due to the low boiling point (905 °C),[29] which was further confirmed by EDX mapping (Figure 2g, Table S1, Figure S4). The resultant XRD pattern (Figure 2a) of CoO_x/NCs shows the presence of the mixture of CoO (35.8°, 41.8° and 60.5°, PDF#15-0806), metallic Co (44.9° and 50.8°, PDF#43-1003), and Co_3O_4 (19.2°, 30.9°, 37.1° and 65.5°, PDF#48-1719),[30] indicating that the Co atoms interact with the O elements from the organic linkers and PVP chains.[31] The Raman spectra also proves the existence of CoO and Co_3O_4, the intensive peak locating at 665 cm^{-1} (Figure 2b) is related to the A_{1g} vibrational mode of Co–O bonds. Another two peaks are accredited to F_{2g} (509.2 cm^{-1}) and E_g (470.5 cm^{-1}) mode corresponding to the combined vibrations of tetrahedral cobalt sites in the Co_3O_4 lattice.[27,32] In addition to the formation of CoO, it is noticed that the intensity of peaks representing Co_3O_4 is decreased in the carbonized samples without PVP polymers. Therefore, it can be deducted that release of oxygen element from PVP polymer increases the cobalt oxidation states. SEM (Figure 2d) image indicates that CoOx/NCs@920 °C possesses a rough surface with abundant CNTs (Figure S2 a), and a porous structure (Figure S2b) when looking at the sheet structure. Furthermore, it is noticed that the large PVP-$Zn_{0.2}$@ZIF-67 particles survive after harsh carbonization process, due to the role of PVP agent. From the HRTEM images (Figure 2e,f) of CoO_x/NCs @920 °C, the existence of CoO surrounded by the graphite layer as well as the formation of CNTs due to the catalytic effect of metallic Co nanoparticles can be observed. The d-spacing values of metallic particles indicate the presence of mixture of CoO and Co_3O_4 where CoO metallic particles are more abundant. Such co-existence of metallic and metal-oxide particle can enhance the conductivity of final products.

Apart from the Co characteristic peaks in XRD pattern, the peak located at 25.0° also proves a higher graphitization degree (Figure 2a) at higher carbonization temperature, which may arise from the incorporation of PVP polymer into ZIFs. Similarly, Raman spectra to investigate the graphitization degree of carbons are shown in Figure 2b. The carbonized PVP-ZIF-8/ZIF67s reveals two graphite characteristic peaks located at 1260 cm^{-1} and 1580 cm^{-1}. In general, these peaks relate to the D band and the G band of graphite.[28] Specifically, D band arises from the defects and disordered atoms in the graphite atomic structure while G band originates from the hybridized sp2 carbon atoms. Such I_D to I_G ratio (I_D/I_G) is an indicator of the graphitization degree.[33] As shown in Figure 2b, the I_D/I_G for CoO_x/NCs without and with PVP are 0.94 and1.08 respectively. The higher I_D/I_G value indicates more defects in the carbonized samples, however, additional 2D and D + D′ band, located at 2670 cm^{-1} and 2930 cm^{-1}, indicate the formation of multilayer graphene in the samples. Hence a better conductivity can be achieved in CoOx/NCs @ 920 °C. The calculated Brunauer-Emmett-Teller (BET) surface area (642.2 $m^2 g^{-1}$) of PVP assisted CoO_x/NCs has been retained well after high temperature carbonization (Figure 2c, Figure S3). This value is significantly larger than those ZIF derived carbons without PVP assistant (51.28 $m^2 g^{-1}$, Figure S3b). Moreover, the pore size distribution indicates that the carbonized sample with PVP assistant

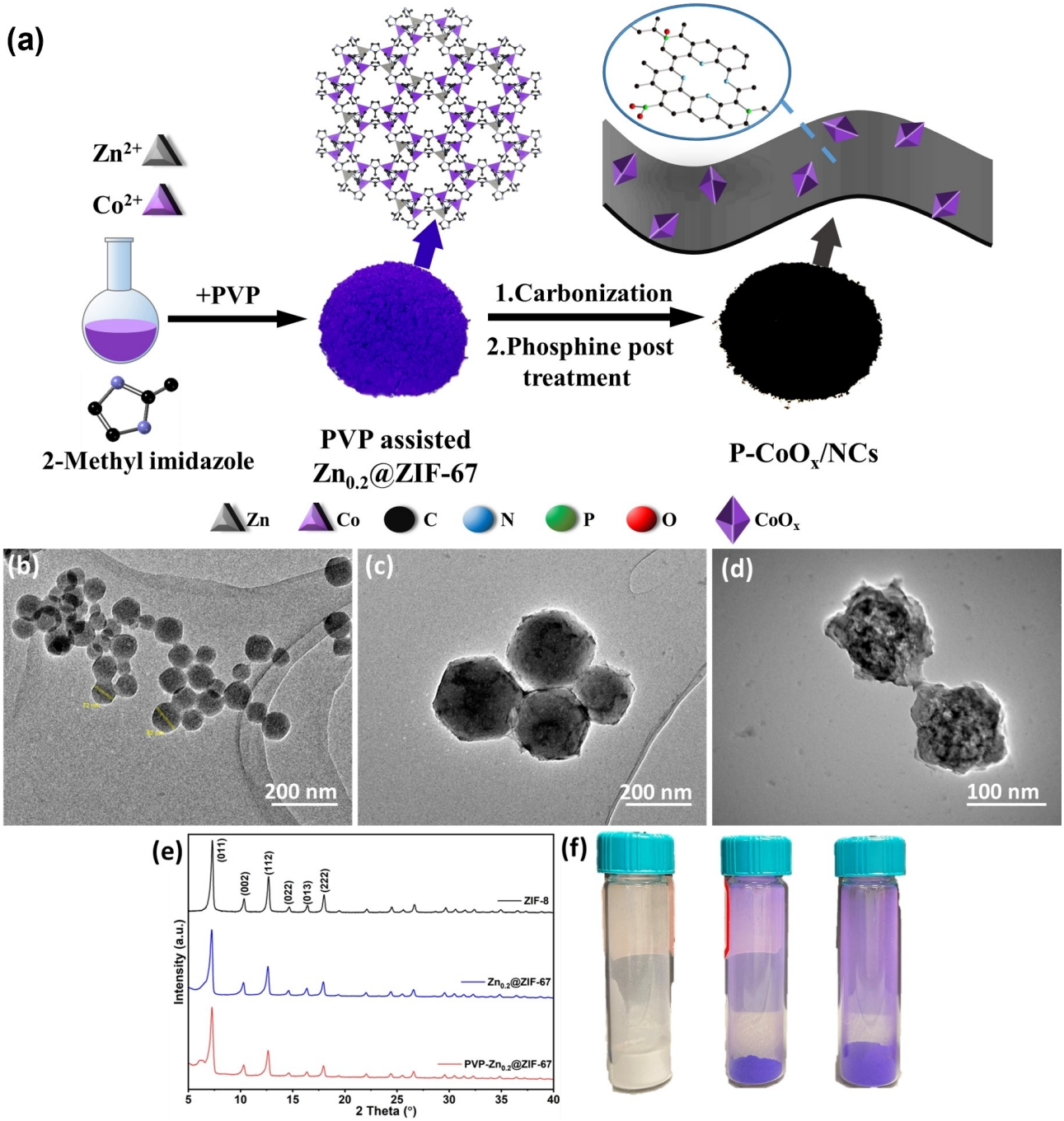

Figure 1. (a) Schematic illustration of synthetic process of P-CoOx/NCs. (b–d) TEM images. (e) XRD pattern. (f) Digital images of ZIF-8, $Zn_{0.2}$@ZIF-67 and PVP-$Zn_{0.2}$@ZIF-67.

generates a micro-mesoporous structure (~3.2 nm in radius, Figure S3c), while those samples without PVP assistance is hard to bear with the breakage of organic linkers at high pyrolysis temperature, only leaving pore system with lower pore volume and smaller pore size (< 0.5 nm in radius, Figure S3d). During the carbonization process, the PVP is supposed to be carbonized firstly.[18] With increasing temperature causing the breakdown of organic linkers of PVP-$Zn_{0.2}$@ZIF-67, a strong confinement pyrolysis effect will be achieved due to the strong cohesive interaction from PVP derived carbons and ZIFs.[27] Thus, the assistance of PVP contributes to the formation of a mesoporous structure and prevents the aggregation of active sites in the samples for further optimization with phosphine.

Morphology and Composition Characterization of P-doped CoOx/NCs

The post phosphine treatments were conducted to manipulate the cobalt electronic environment. SEM images (Figure 3a–c)

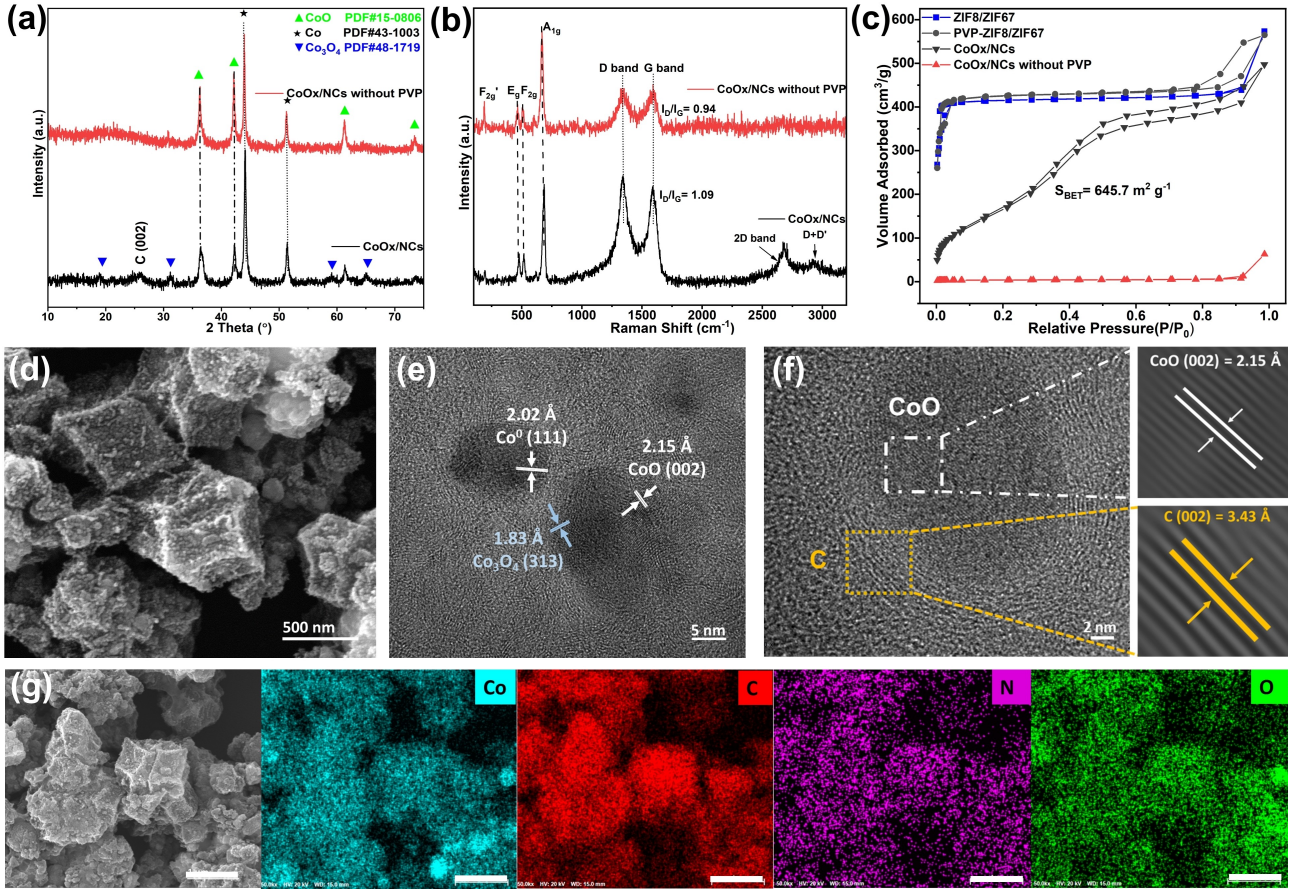

Figure 2. (a) XRD pattern, (b) Raman spectrum of CoOx/NCs with and without PVP polymer at 920 °C; (c) N_2 adsorption and desorption isotherm of ZIFs before and after carbonization, as well as the role of PVP capping agent @920 °C; (d) TEM image of CoOx/NCs@ 920 °C; (e–f) corresponding HRTEM images (Enlarged: inverse FFT image of C and CoO lattice plane); (g) EDS mapping of CoOx/NCs@920 °C (Scale bar: 1 μm).

reveals that few amount (600 and 900 mg) of phosphine treatment exhibit limited morphology changes, while the high input of phosphine gases cause the surface corrosion, leading to a smooth surface in 1200 P-CoOx/NCs. TEM image (Figure 3d and S5a,b) of 900 P-CoO_x/NCs indicate abundant carbon shells existed in sample surface, where cobalt nanoparticles are wrapped. HRTEM (Figure 3e) exhibited a clear multilayer graphene structure outside the exposed cobalt nanoparticles, as a result, preventing the formation of CoP nanoparticles. The SAED pattern (Figure 3f) shows a polycrystalline structure of 900 P-CoO_x/NCs. Further EDS mapping (Figure 3g and Table S2) of 900 P-CoO_x/NCs confirms the unfirm of P element with an atomic concentration of 2.21 % into the carbon frameworks.

XRD pattern (Figure 4a) of P-CoOx/NCs samples indicates little changes in the CoO and metallic Co phases after phosphine treatment. Raman spectrum of corresponding P-CoO_x/NCs (Figure 4 < xfigr4b) reveals that the decreased intensity of A_{1g}, F_{2g} and E_g vibration of Co tetrahedral site, arising from the surface corrosion effect of phosphine gases. To further reveal P doping effects in carbon shells, UPS was conducted to investigate the Fermi level of 900 P-CoO_x/NCs. As indicated (Figure 4c), the cut-off energy of CoO_x/NCs and 900 P-CoO_x/NCs are 12.21 eV and 12.56 eV, respectively. By using following equation: $E_f = \varphi_m = h\nu - E_{cut-off}$, the Fermi levels of samples were determined to be 9.01 eV and 8.66 eV, correspondingly. Further plot (Figure 4f) shows that the Fermi level of 900 P-CoO_x/NCs shifts towards higher level, compared with that of CoO_x/NCs. This shift can be attributed to the P doping at carbon frameworks, which further redistribute the electronic environment of cobalt elements. Moreover, when samples are contacted with electrodes, electrons can be more easily transferred to 900 P-CoO_x/NCs, facilitating further catalytic reactions.

The X-ray photoelectron spectroscopy (XPS) was employed to investigate the surface chemical states, prove the interfacial charge transfer from Co to P and confirm the P doping into the carbon framework instead of the direct interaction with Co element. In the whole XPS spectrum, it is noticed that there is still little amount of Zn in the samples and the most abundant part is graphite carbons (Figure S8). Typically, in Table 1, the atomic amount of Zn accounts for 0.11 % and 69.86 % of signals arise from carbons. When considering the phosphine treatment, it can be revealed that with increasing amounts of phosphate precursor, the atomic percentage of P at the surface of m P-CoO_x/NCs shows the similar trend by increasing from 6 % to 11.26 % indicating the successful phosphine post treatment. It is also noticed that the P 2p spectrum is deconvoluted into P–O (133.9 eV) and P–C (132.2 eV). With respect to C 1s spectrum, the relevant C–P is attributed to 286.5 eV (Figure S8 c,d).[34,35]

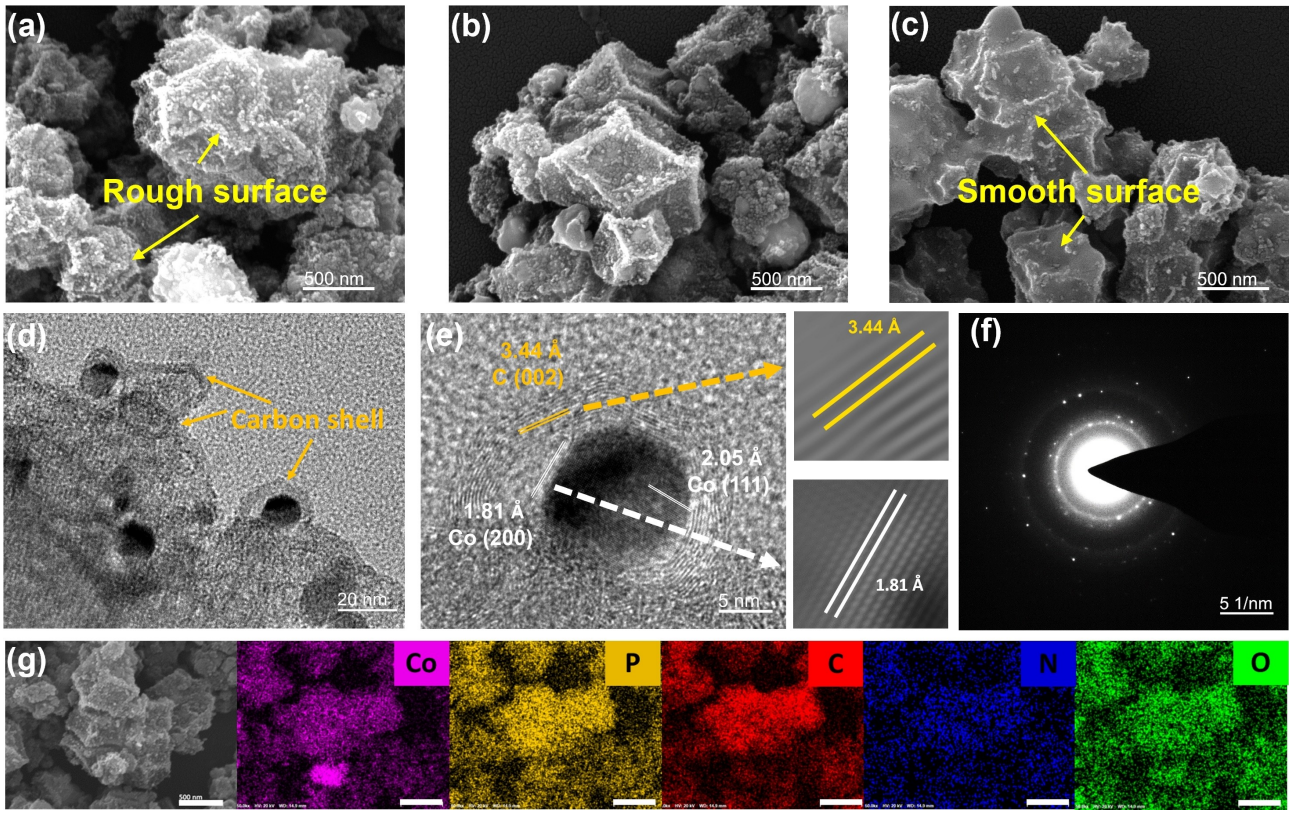

Figure 3. (a–c) SEM images of CoO_x/NCs treated with different amounts (600 mg; 900 mg and 1200 mg). (d) TEM image. (e) HRTEM (adjacent: inverse FFT images). (f) Selected area diffraction and (g) EDS mapping of 900 P-CoO_x/NCs (Scale bar: 500 nm).

Table 1. Surface Element Composition (XPS) of the P-treated ZIF derivates.

	XPS atomic % (at. %) [a]						
Sample	C	N	O	Zn	Co	P	$Co^{3+}/Co^{2+}/Co^{0}$
CoO_x/NCs	69.86	2.41	25.59	0.11	2.03	-	1: 056: 0.53
600 P-CoO_x/NCs	66.08	2.48	22.96	0.15	2.33	6.00	1: 0.63: 0.47
900 P -CoO_x/NCs	62.56	2.49	24.39	0.12	3.12	7.32	1: 1.17: 0.91
1200 P- CoO_x/NCs	58.58	2.45	27.36	0.17	3.05	8.39	1: 0.71: 0.39

[a] Surface atomic percentage derived from high-resolution C 1s, O 1s, N 1s, Zn 2p, Co 2p and P 1s core-level peaks.

For comparison, we conduct the same phosphorization process on CoO_x/NCs samples without PVP assistance. As shown in Figure S7, the large particles are observed at CoO_x/NCs framework surface. Moreover, XRD pattern confirms the crystal phase. Those peaks observed at 31.3°, 36.3°, 45.8°, 47.9°, 51.8° 56.4° are assigned to cobalt phosphide phase (PDF# 29-0497). Combined with XPS results, it is confirmed that PVP derived carbons may function as protective shell, which further prevents the phosphorization of metallic cobalt and cobalt oxide.

In addition to the surface chemical composition analysis, the interfacial charge transfers between Co and P atoms are confirmed by comparing the high-resolution Co 2p peaks and P 2p spectrum (Figure 4d.e). It is noticed that the spectrum of 900P-CoO_x/NCs is predominant of spin-orbit doublets (Co $2p_{3/2}$ and Co $2p_{1/2}$) as well as shakeup satellites, characteristics of mixed valence of Co^{2+}/Co^{3+}.[36,37] The spectrum is further deconvoluted into Co^{3+} (781.1 eV), Co^{2+} (783.2 eV), Co^{0}(780.3 eV) with a Co^{3+} to Co^{2+} to Co^{0} ratio of 1:1.17:0.91. The peaks located at 780.3 eV and 796.2 eV are attributed to

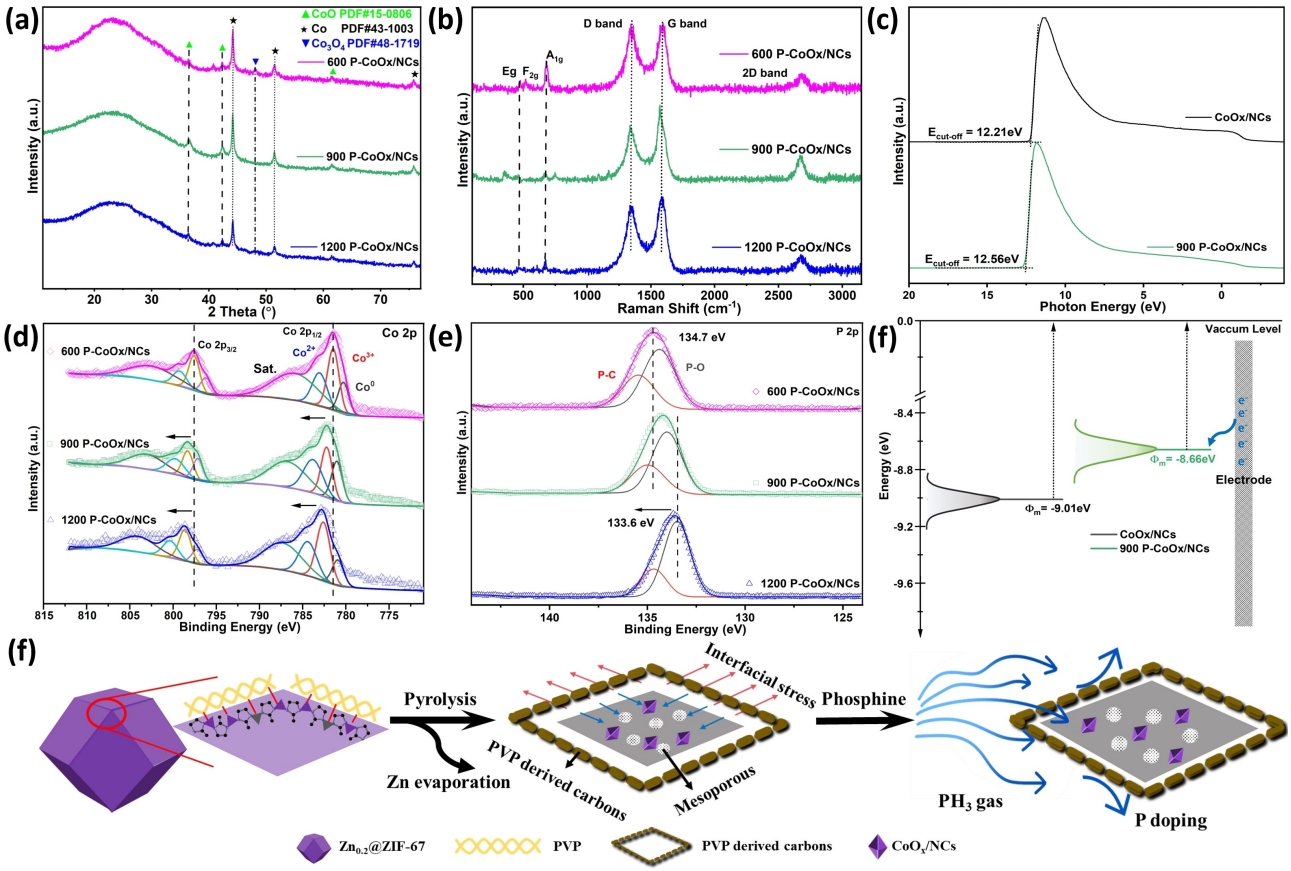

Figure 4. (a) XRD pattern, (b) Raman spectrum of 600 P, 900 P, 1200 P-CoOx/NCs. (c) Ultraviolet photoelectron spectroscopy (UPS) of CoOx/NCs and 900 P-CoOx/NCs. (d) Co 2p spectrums. (e) Corresponding P 2p spectrums of 600 P, 900 P, 1200 P-CoOx/NCs. (f) Schematic illustration of PVP role in carbonization and phosphine post treatment.

the Co^0. Interestingly, the 900P-CoO_x/NCs possesses highest Co^{2+} fraction among all prepared samples (shown in Table 1), arising from the reducing ability of phosphine gas. Several studies[37–39] have shown that excessive amount of PH_3 gas during phosphorization proves will further reduce CoP to Co_2P,[40] forming heterojunctions. Compared with the Co 2p spectrum of 1200P-CoO_x/NCs, a positive shift towards higher binding energy from 600P-CoO_x/NCs was observed (~0.8 eV). Accordingly, high resolution of P 2p spectrum shows a negative shift (134.7 eV to 133.6 eV) due to the increase in the electron density. This shift arises from the electronic transfer from Co to P atom, due to the stronger electron affinity of P.[41]

As shown in O1s spectrum (Figure S8b), the peak representing the Co–O bond (528.7 eV) vanishes after the P vapor treatment. This phenomenon could be the excessive P element on the surface of sample hindering the signal of Co–O. Combined with the information from P 2p spectrum (Figure S8d), it can be concluded that phosphorus atoms are introduced to carbon frameworks instead of having direct interactions with Co to form CoP as no spin-orbital doublets are observed in all x P-CoO_x/NCs. While for those O elements in cobalt oxide, it cannot be substituted by P to form CoP due to the strong ionic bonding of cobalt oxide. When considering the configurations of N atom of CoO_x/NCs, its 2p spectrum is divided into three configurations:[42,43] pyridinic N (398.0 eV), pyrrolic N (403.2 eV) and N oxide (405.5 eV) with an atomic percentage of 46.6%, 45.2%, and 8.2% respectively. When introducing phosphorus atoms into carbon frameworks, it can be noticed (Figure S8 c), an increase in the amount of pyrrolic N and correspondingly a decrease in the percentage of pyridinic N suggesting P atoms are introduced into carbon frameworks with similar configuration of pyridinic N.[44] The presence of different nitrogen configurations also provides the possibility to coordinate with metallic actives forming M-N_4 structure which has been reported to facilitate the OER.[45]

As indicated in Figure 4f, it can be concluded that the excessive amount of PVP is incorporated into ZIF frameworks. Meanwhile, PVP polymers form layers on surface of ZIFs, due to their affinity to metal atoms. The role of PVP polymer is further summarized as follows: 1. The PVP layer contributes to the formation of carbon layers during pyrolysis process. The PVP derived carbons not only increase the graphitization degree of final products, but also provide interfacial stress, preventing the inward collapse of ZIF frameworks. 2. The carbon out layers further function as protective shells, which sluggish the phosphorization process. Combined with XRD and XPS results, instead of the formation of CoP, the P atoms mainly substitutes

the C and N atoms, forming P–C bonds and PO_4^{3-} species in the carbon frameworks.

Electrocatalytic Evaluation

Based upon above explanation of PVP role, we further optimized the Zn/Co ratios in ZIF frameworks in water splitting (Figure S9–12). With well-constructed pore systems based on carbonized PVP assisted $Zn_{0.2}$@ZIF-67, the electrocatalytic activities of phosphine treated CoO_x/NCs were evaluated in N_2 saturated 1 $_M$ NaOH at ambient conditions with a sweep rate of 5 mV/s. The reference Pt/C (20 wt%) catalyst was evaluated as benchmark for HER. It possesses an overpotential of 20 mV at current density of 10 mA cm^{-2} and a Tafel slope of 35 mV/dec in 1 $_M$ NaOH (Figure S13a), due to its fast proton absorption and hydrogen desorption. Among all samples, CoO_x/NCs possess the poorest catalytic performance, while 900P-CoO_x/NCs present low overpotential and low Tafel slope. Due to its optimized electronic environment, Co element exhibit outperforming activities in 900P-CoOx/NCs with an overpotential of 82 mV at 10 mA cm^{-2} (Figure 5a) and a Tafel slope of 79 mV/Dec (Figure 5b). This Tafel slope of 79 mV/Dec indicates the rate-determining step (RDS) as Volmer-Heyrovsky step, where electron transfer and hydrogen desorption sluggish the whole reaction pathway.[18] Nyquist plot was conducted at an overpotential of 100 mV to investigate the electron transfer ability (R_{CT}). As indicated in Figure 5c, commercial Pt/C exhibits a low R_{CT} of 12.5 Ω, followed by 900 P-CoO_x/NCs (R_{CT} = 18.2 Ω), 1200 P-CoO_x/NCs (R_{CT} = 23.0 Ω), 600 P-CoO_x/NCs (R_{CT} = 27.7 Ω). The smaller value of 900 P-CoOx indicates the easier electron transferability towards adsorbed hydrogen atoms.

Similar to the HER results, the OER performance of 900P-CoO_x/NCs also outperforms those samples treated with 600 mg and 1200 mg of P precursors. As shown in Figure 5 d, its overpotential required to achieve a current density of 10 mA cm^{-2} is 343 mV and a 383 mV to achieve the current density of 50 mA cm^{-2}, while others exhibit higher overpotentials (η_{10} = 390 mV and 400 mV for 600P and 1200P-CoO_x/NCs correspondingly. The Tafel slope of 900P-CoO_x/NCs possesses

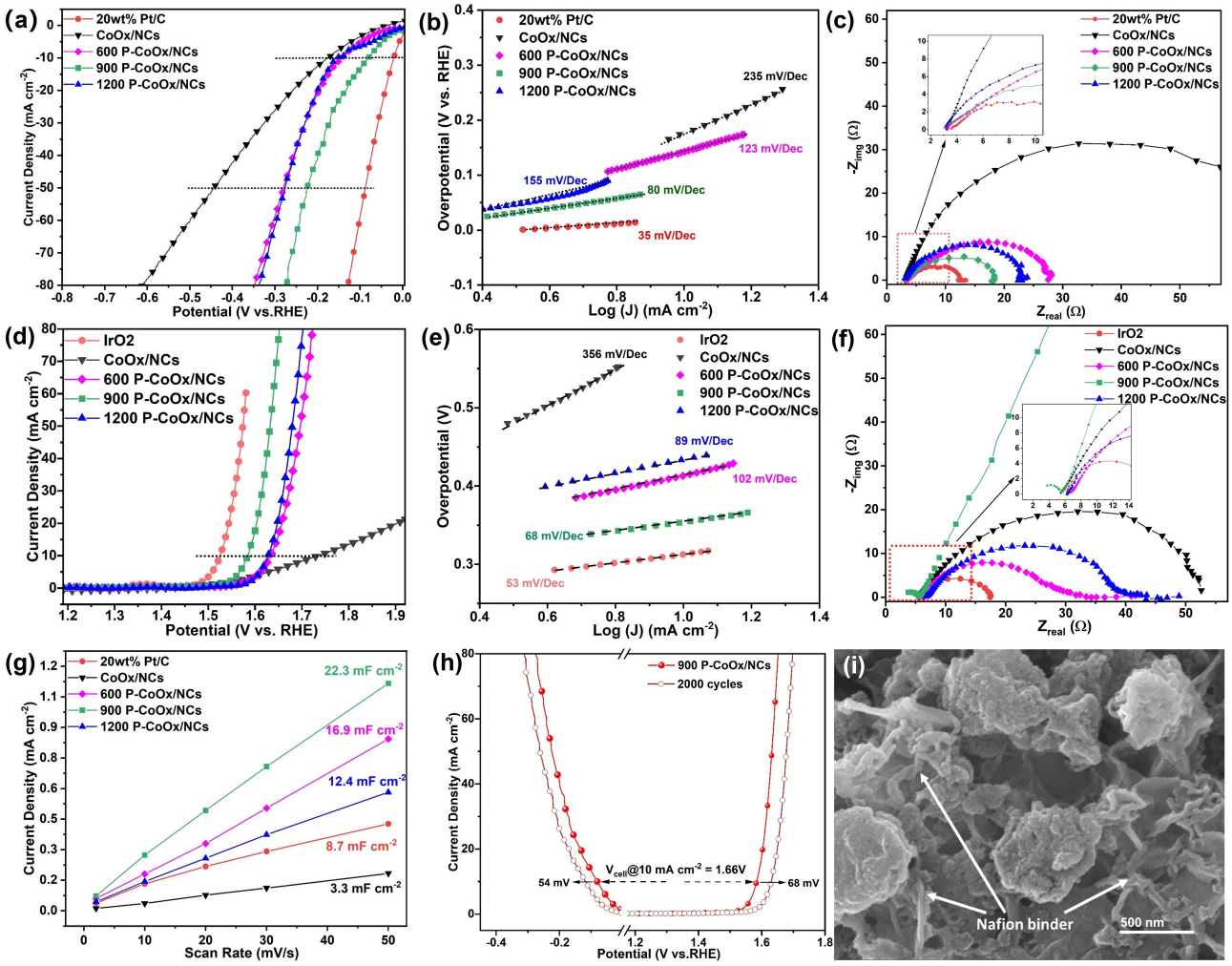

Figure 5. (a) HER polarization curves. (b) Corresponding Tafel slope and (c) Nyquist plot of CoO_x/NCs treated with 0, 600, 900, 1200 mg of P precursors and 20 wt% Pt/C benchmark at a sweep rate of 5 mV/s. (d) OER polarization curves. (e) Corresponding Tafel slope and (f) Nyquist plot of CoO_x/NCs treated with 0, 600, 900, 1200 mg of P precursors and IrO_2 benchmark at a sweep rate of 5 mV/s in 1$_M$ NaOH. (g) Double layer capacitance. (h) LSV curves of 900 P-CoO_x/NCs after cycling; (i) SEM image of 900 P-CoO_x/NCs after cycling.

lowest value of 68 mV/Dec (Figure 5e), indicating the highest kinetics in OER. The Nyquist plot was then conducted at an overpotential of 100 mV to demonstrate the resistance of electron transfer, where a lower value indicates a faster electron transfer process (Figure S15).[46] All the semicircles in Figure 5f deviate the origin point with a value of ~6.5 Ω, caused by the electrolyte resistance (R_S). Among all samples, 900P-CoO_x/NCs possess the lowest electron transfer resistance (2.5 Ω). This value suggests 900P-CoO_x/NCs can facilitate the charge transfer (R_{CT}) at the interface towards oxygen evolution, due to a moderate electronic environment of Co elements. While other phosphine treated samples exhibit relatively larger resistance to the charge transfer (27.5 Ω for 600P-CoO_x/NCs; 39.2 Ω for 1200P-CoO_x/NCs). The larger resistance can be contributed to the weaker or stronger interaction between Co and P with undesired electronic environment of Co element. However, compared with the R_{CT} of CoO_x/NCs (49.5 Ω), the treatment with phosphine vapor improves the electron transfer resistance as well as exposed active sites in the carbonized sample.

Double layer capacitance (C_{dl}) measured at non-faradic region was employed to investigate the possible active sites in the samples (Figure 5g and S14). The calculated values of C_{dl} are 3.3 mF cm^{-2}, 16.9 mF cm^{-2}, 22.3 mF cm^{-2}, 8.7 mF cm^{-2} for CoO_x/NCs, 600P-CoO_x/NCs, 900P-CoO_x/NCs, 1200P-CoO_x/NCs and commercial Pt/Cs respectively. Among them, 900P-CoO_x/NCs present the highest C_{dl} value, suggesting more active sites exposed for the proton adsorption. Compared with the C_{dl} of CoO_x/NCs, all values of P-CoO_x/NCs are larger, suggesting the P treatment is an effective strategy to expose the available active sites. Since our P-CoO_x/NCs (~2.5×10^{-7} mol/cm^2) has higher active site density than even Pt/C product (~2.1×10^{-7} mol/cm^2), the catalyst carbon matrix in our samples would be obviously superior to the carbon substrate of Pt/C. This advantage is attributed to its mesoporous pore size (rather than micro pore of Pt/C). As a result, this post phosphorus doping strategy significantly improves the reaction kinetics of samples. In addition, it is noticed that the higher Co^{2+} fraction in the sample boosting the overall reaction suggesting the Co^{2+} are the active sites towards water splitting.[27,30] The polarization curves towards HER and OER after 2000 CV cycles (Figure 5h) also prove a good stability of as-synthesized samples with a deterioration of 54 mV (HER) and 68 mV (OER) at the current density of 10 mA cm^{-2}. Meanwhile, SEM (Figure 5i), XRD and Raman spectrum (Figure S16b,c) confirms the morphological and structural stability after the cycling test.

The overall water splitting reaction was conducted by drop-casting catalysts on the carbon paper as cathode and anode. As demonstrated in Figure 6a, the fabricated two-electrode cell requires a rather low voltage (1.69 V) to achieve a current density of 10 mA cm^{-2}. The stability of this cell was further tested at 1.69 V for 15 hours. It is noticed that a 4.7% of current density decay, which is likely attributed to the protective graphite layers around the cobalt oxides (Figure 6b). To further explore the catalytic performance of 900 P-CoO_x/NCs, the production of H_2 and O_2 as a function of reaction time was collected and has a good consistence with theoretical calculated amount H_2 and O_2 production at the current density of 9.5 mA cm^{-2}. The water splitting reaction based on 900P-CoO_x/NCs achieves an average Faraday Efficiency above 95% with a ratio of H_2 to O_2 equalling to 2 (Figure S19a–b and Table S3). Moreover, the production rate for H_2 and O_2 are calculated to be 0.048 μmol s^{-1} and 0.024 μmol s^{-1} respectively. What's more, our 900 P-CoOx/NCs exhibits a good position in both HER and OER catalytic performance compared with other cobalt based catalysts (Figure S20).

Investigation of Catalytic Performance of Multivalence Co

To reveal the role of different valence states of cobalt in P-CoO_x/NCs, a series of post treatments have been conducted: (1) Employ acid to remove cobalt oxide denoting Co/NCs; (2) Anneal CoO_x/NCs at 550 °C to transform metallic Co to cobalt oxide, referring to O–CoO_x/NCs. As shown in Figure S17a,b, the acid treated CoOx/NCs exhibits an open-structure, caused by the strong acid leaching effect. While the oxidized samples reveal random particle distribution. Moreover, the carbon content of O–CoOx/NCs is rarely observed, due to the open-air

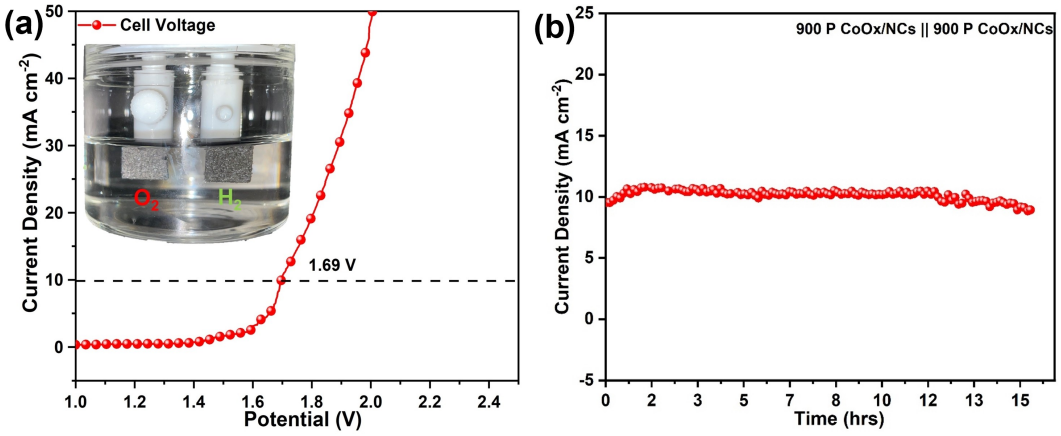

Figure 6. (a) Cell voltage of overall water splitting reaction (900 P-CoO_x/NCs | | 900 P-CoO_x/NCs). (b) Chronopotentiometry curve for 900P-CoO_x/NCs at 1.69 V vs. RHE.

calcination. Further XRD pattern (Figure 7a) and Raman spectrum (Figure 7b) confirm the observation. The new peaks in O–CoOx/NCs represent the existence of Co_3O_4, indicating a higher oxidation fraction of Co. For acid leached sample, only characteristic peaks of metallic cobalt are identified, proving a lower oxidation state. When considering HER performance (Figure 7c), CoO_x/NCs requires the lowest overpotential (219 mV) compared with that of oxidized CoO_x/NCs (302 mV), and metallic Co/NCs (235 mV) to achieve a current density of 10 mA cm^{-2}. This phenomenon indicates the presence of metallic Co (Co^0) cooperating with higher valence state of cobalt (Co^{2+}) lowers the energy barrier of hydrogen generation. However, all Tafel slopes of corresponding samples towards HER are above 150 mV/Dec suggesting the desorption of H_{ads} are the rate-determining steps[47] in the alkaline medium. Nevertheless, Co/NCs at higher current density exhibits a faster reaction kinetics, which can be attributed to the open structure of carbon frameworks and more exposed metallic active sties.

When considering OER performance (Figure 7d), both acid-treated and oxidized CoO_x/NCs (Co/NCs and O–Co/NCs) requires a higher overpotential to achieve the current density of 10 mA cm^{-2} (470 mV and 427 mV respectively). This higher overpotential prove the synergetic effects between Co^{2+} and Co^{3+} to boost the water splitting reaction. Interestingly, the C_{dl} value of Co/NCs shows the highest value among all three batches (6.75 mF/cm^2, Figure S17) which may arise from the removal of excessive metal oxide and amorphous carbons. This acid leaching process provides more possibilities with active sites exposed to electrolyte. It is also noticed that the reaction kinetics of O–CoOx/NCs has been improved for both HER and OER. This enhancement may be attributed to the oxidation of Co^{2+} to Co^{3+} firstly then followed by the formation of key intermediate Co–OOH by OH^- adsorption during the water oxidation reaction.[48] When considering electron transfer resistance of multivalent Co elements. The existence of various states of cobalt in CoO_x/NCs shows the lowest value (49.5 Ω, Figure S17) suggesting the synergetic effects between cobalt elements and the as-prepared CoO_x/NCs can be employed as a promising candidate for post phosphine treatment.

Upon abovementioned analysis, here are four reasons contributing to this effective electrocatalyst: 1) The carbonization of ZIF-8/ZIF67 assisted by PVP remains a micro-meso porous system contributing to active sites exposure, and the pyrolysis of organic linkers provides N doping into the carbon framework facilitating the OER; 2) The micro-mesoporous system and PVP functionalization promotes the surface interaction between phosphine vapor and carbons to allow P doping. As a result, the optimized electronic environment of cobalt oxides tuned by N and P heteroatoms towards boosting water splitting reaction; 3) Phosphine post treatment enhances the accessible electrochemical active surface area as well as the electron transfer kinetics shedding lights on the electronic modulation of ZIFs assisted by PVP; 4) The synergetic effect between Co^0 and Co^{2+} facilitates HER kinetic, meanwhile, effect between Co^{2+} and Co^{3+} improve the OER kinetics.

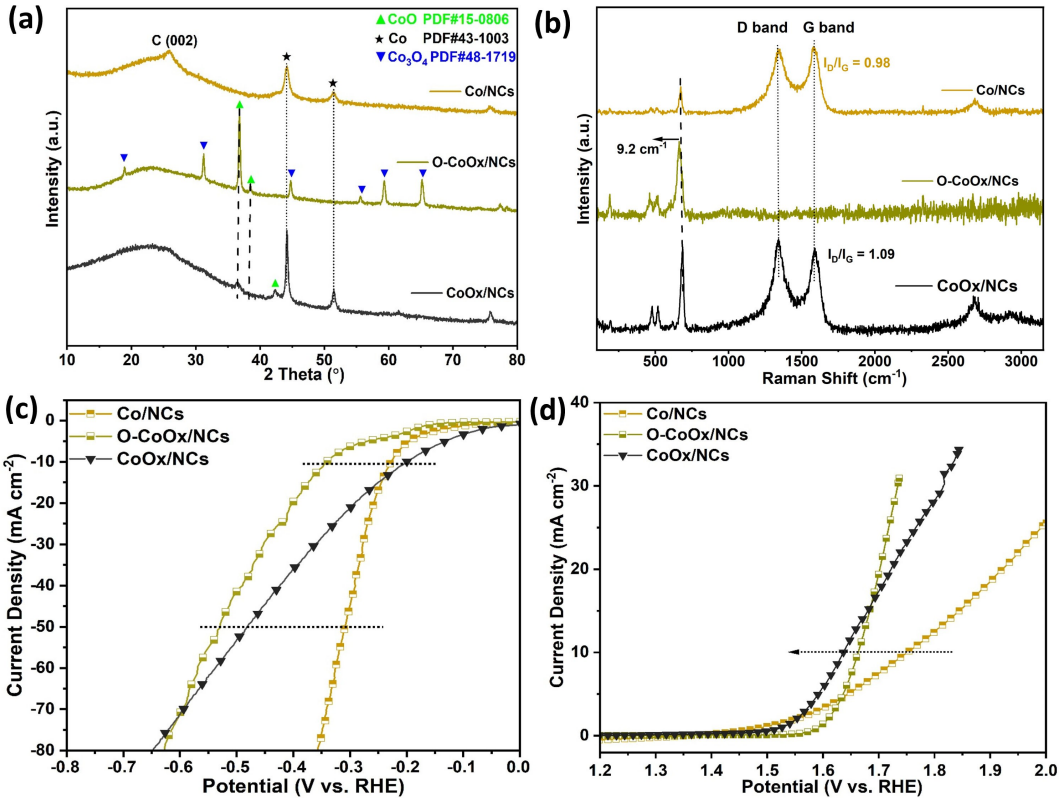

Figure 7. (a) XRD pattern; (b) Raman spectrum; (c) HER; and (d) OER polarization curves of Co/NCs, O–CoO_x/NCs and CoO_x/NCs.

Conclusion

In conclusion, we fabricated the N/P codoped cobalt oxide based electrocatalyst to boost the water splitting reaction, the N atoms originated from organic linkers and P elements from phosphine vapor were doped into the carbon framework, which successfully influence the electronic environment of cobalt oxides. Moreover, the PVP assisted carbonization process allows the catalyst possessing a high specific surface area of 642.5 $m^2 g^{-1}$ and a micro-mesoporous system. Based on the abovementioned strategies, different amounts of phosphine treatments allow the optimization in electrocatalytic performance. The final electrocatalyst can drive the HER and OER at a current density of 10 mA cm^{-2} at an overpotential of 89 mV and 343 mV respectively. The acid and oxidation post treatment reveal that the synergetic effect between metallic Co, Co^{2+}, and Co^{3+} boosts the water splitting reaction. In addition, the constructed electrolyzer based on 900P-CoO_x/NCs possesses a cell voltage of 1.69 V to achieve the current density of 10 mA cm^{-2}.

Experimental Section

Materials

All materials were purchased and used without further purification. Zinc nitrate hexahydrate ($Zn(NO_3)_2 \cdot 6H_2O$, ≥98.0%), 2-methylimidazole (2-MeIM, ≥97.0%), sodium hypophosphite monohydrate (NaH_2PO_2) and 20 wt% Pt/C were purchased from Alfa Aesar. Cobalt nitrate hexahydrate ($Co(NO_3)_2 \cdot 6H_2O$, ≥98.0%) and polyvinyl pyrrolidone (PVP, Mw = 13 kDa) were purchased from Aladdin. Methanol and ethanol (ACS grade) were purchased from Anaqua Co Ltd..

Synthesis of $Zn_{0.2}$@ZIF-67 and PVP-$Zn_{0.2}$@ZIF-67

In a typical synthesis of $Zn_{0.2}$@ZIF-67[20], $Zn(NO_3)_2 \cdot 6H_2O$ (0.36 g) and $Co(NO_3)_2 \cdot 6H_2O$ (1.45 g) was completely dissolved in 50 mL of methanol to form a purple solution A. 2-Methylimidazole (2-MeIM, 4.49 g) was dissolved in 93.3 mL of methanol to form a homogeneous solution B. Then the solution B was poured into solution A under stirring for 1 hour (in total 143.3 mL of methanol). The resultant powders were collected under 5000 rpm centrifuge and washed with methanol three times to remove unreacted materials and dried in vacuum at 60 °C for 8 hours.

To fabricate PVP assisted $Zn_{0.2}$@ZIF-67[35], an additional methanolic PVP solution (1.8 g of PVP dissolved in 30 mL methanol) was poured into abovementioned metal precursor and organic linker contained methanolic solution ($Zn_{0.2}$@ZIF-67) after 20 minutes' nucleation of ZIFs. Finally, the obtained PVP assisted $Zn_{0.2}$@ZIF-67 s underwent washing with methanol for three times and were dried in vacuum at 60 °C overnight.

Synthesis of P-doped CoO_x/N-doped Carbons (CoO_x/NCs)

The synthesized PVP assisted $Zn_{0.2}$@ZIF-67 further experienced the carbonization process at 920 °C for 150 minutes with a ramp rate of 5 °C/min under N_2 atmosphere and was naturally cool down. The resultant products were denoted as CoO_x/N-doped carbons (CoO_x/NCs). In this work, all the carbonizations were employed on the PVP assisted $Zn_{0.2}$@ZIF-67 samples. Otherwise, the direct carbonization of $Zn_{0.2}$@ZIF-67 at 920 °C for 150 minutes denotes CoO_x/NCs without PVP.

After the carbonization, different amounts of NaH_2PO_2 (x = 600, 900, 1200 mg) were employed as phosphine precursors to conduct the surface treatment of CoO_x/NCs. In a typical treatment, 5 mg of CoO_x/NCs was placed in the downstream of a porcelain boat and x (600, 900, 1200) mg of NaH_2PO_2 was put in the upstream of the boat under N_2 atmosphere. The temperature of tube furnace was elevated with a ramp rate of 3 °C/min to 350 °C and maintained for 120 minutes, allowing the decomposition of NaH_2PO_2 (Eq. 1, Notice: the tail gas of NaH_2PO_2 is extremely toxic requiring saturated $CuSO_4$ solution as exhaust converters). The final products were collected after the naturally cool down of the furnace which were denoted as m P-CoO_x/NCs where m = 0, 600, 900, 1200.

$$2\ NaH_2PO_2\ (s) \rightarrow PH_3\ (g) + Na_2HPO_4\ (s) \quad (1)$$

Preparation of Co/NCs and Oxidized CoO_x/NCs (O–CoO_x/NCs)

To prepare Co/NCs, CoOx/NCs powders (100 mg) were dispersed into 5 M HCl (50 mL) for 2 days[45,46] by undergoing following Eqs. 2 and 3. These processes transform cobalt oxide to soluble $CoCl_2$. The resultant products were washed with DI water and methanol three times to wash away $CoCl_2$ and denote Co/NCs.

$$Co_3O_4(s) + 8HCl(l) \rightarrow 3CoCl_2(l) + 4H_2O(l) + Cl_2(g) \quad (2)$$

$$CoO(s) + 2HCl(l) \rightarrow CoCl_2(l) + H_2O(l) \quad (3)$$

To obtain oxidized CoO_x/NCs (O–CoO_x/NCs), CoO_x/NCs powders (100 mg) were put into the crucible in a tube furnace in air. The temperate was risen to 550 °C with a ramp rate of 5 °C/min and kept for 2 hours. During this process, the metallic Co will be transformed to the Co^{2+} and Co^{3+}. The final products were collected after naturally cooling down of the furnace.

Preparation of Catalysts on the Carbon Paper

The as-synthesized xP-CoO_x/NCs (5 mg) was dispersed in a mixture of 2-proponal (250 μL) and DI water (750 μL, conductivity = 0.26 μS cm^{-1}). At the meantime, Nafion solution (30 μL, 5 wt%) was dropped into the above solution. After 1 hour sonication to achieve a uniform dispersion, 20 μL of prepared ink was drop-cast onto the 0.5×0.5 cm^2 carbon paper and dried under infrared irradiation for 30 minutes to yield a mass loading ~0.2 mg/cm^2.

Physical Characterization

Scanning electron microscopy (SEM) images and Energy Dispersive X-ray spectrometer (EDX) of composition analysis were obtained from a Tescan VEGA3, Czech (accelerating voltage = 20 kV). Transmission electron microscopy was conducted on JEOL 2100F, Japan (operating voltage = 200 kV). X-ray diffraction (XRD) patterns were collected on a Rigaku SmartLab 9 kW-Advance, Japan using monochromate Cu kα radiation (λ = 0.154 nm) at a scan rate of 7°/min. Raman spectroscopy was taken using a NomadicTM 3-in-1 microscope, America with He–Ne laser excitation (λ = 532 nm) and OLYMPUS MPlanFLN 10x objective lens. Brunauer-Emmett-Teller (BET) surface area measurements were taken by N_2 adsorption-desorption isotherm at 77 K using NOVA touch LX4, Austria. X-ray photoelectron spectroscopy (XPS) was recorded on a Thermo

Scientific Nexsa using a monochromatic and focused Al Kα source (1486.6 eV). Ultraviolet photoelectron spectroscopy (UPS) was conducted on a Thermo ESCALAB 250XI, using He I source (21.22 eV).

Electrochemical Measurements

The electrochemical measurements were carried at the electrochemical workstation (CHI660D, Shanghai Chenhua Science Technology Corp., Ltd.) at room temperature. A typical three-electrode configuration including Pt plate (1×1 cm^2, 0.1 mm) as counter electrode; Ag/AgCl (saturated KCl solution) as reference electrode, carbon paper (0.5×0.5 cm^2) as working electrode was employed for both HER and OER half reaction evaluations. In this case, N_2 saturated 1 M NaOH (pH = 13.6) was functioned as electrolyte. The linear sweep voltammetry (LSV) was measured at a scan rate of 5 mV/s with 85% iR compensation. All recorded potentials were converted to the reversible hydrogen electrode (RHE) according to the Nernst equation (Eq. 4):

$$E_{RHE}(V) = E_{working} + 0.059pH + E^0_{Ag/AgCl} \quad (4)$$

Where E_{RHE} is the calculated potential vs. RHE, $E_{working}$ is the recorded potential against Ag/AgCl, and $E^0_{Ag/AgCl}$ equals to 0.197 V which is the standard equilibrium potential at 25 °C.

The Tafel slope has been plotted according to the equation below (Eq. 5) to investigate the reaction kinetics:

$$\eta = a + \beta \log(j) \quad (5)$$

Where η and j are overpotential (V) and current density (mA cm^{-2}) respectively, and other symbols represent their usual meanings.

Double layer capacitance (C_{dl}) was taken by employing cyclic voltammetry (CV) at scan rates varying from 2 mV/s to 50 mV/s. The C_{dl} was calculated by figuring out the potential difference in the non-Faradaic region. Electrochemical Impedance Spectroscopy (EIS) measurements were conducted at an overpotential of 20 mV for HER and 100 mV for OER with an amplitude of 5 mV from 100 KHz to 0.1 Hz to investigate the charger transfer resistance and solution resistance at high- and low-frequency region respectively.

The stability test was conducted by the chronoamperometric curves (I-t) at a current density of 10 mA cm^{-2}, and the CV testing with a scan rate of 50 mV s^{-1} for 700 cycles. The electrolyzer for overall water splitting reaction was composed of two same electrodes where both cathode and anode are made of carbon paper (1×1 cm^2) with 900 P-CoO_x/NCs (mass loading ~0.2 mg cm^2, 900P-CoO_x/NCs||900P- CoO_x/NCs).

Acknowledgements

We acknowledge the funding supports from PolyU RCRE (1-BBCB) and RI-IWEAR (1-CD8E).

Conflict of Interests

The authors declare no conflict of interests.

Data Availability Statement

The data that support the findings of this study are available from the corresponding author upon reasonable request.

Keywords: metal-organic frameworks · heteroatom doping · mesoporous carbons · phosphine modulation · water splitting reaction

[1] J. Zhu, L. Hu, P. Zhao, L. Y. S. Lee, K. Y. Wong, *Chem. Rev.* **2020**, *120*, 851–918.
[2] Q. Wang, D. Astruc, *Chem. Rev.* **2019**, *120*, 1438–1511.
[3] R. Tong, K. W. Ng, X. Wang, S. Wang, X. Wang, H. Pan, *J. Mater. Chem. A* **2020**, *8*, 23202–23230.
[4] J. Yang, Y. Xiao, Q. Zhao, G. Zhang, R. Wang, G. Teng, X. Chen, M. Weng, D. He, S. Mu, Y. Lin, F. Pan, *Nano Energy* **2019**, *59*, 443–452.
[5] S. Ma, M. Sadakiyo, M. Heim, R. Luo, R. T. Haasch, J. I. Gold, M. Yamauchi, P. J. A. Kenis, *J. Am. Chem. Soc.* **2017**, *139*, 47–50.
[6] X. Zhang, X. Yu, L. Zhang, F. Zhou, Y. Liang, R. Wang, *Adv. Funct. Mater.* **2018**, *28*, 1706523.
[7] Z. Shen, Y. Zhuang, W. Li, X. Huang, F. E. Oropeza, E. J. M. Hensen, J. P. Hofmann, M. Cui, A. Tadich, D. Qi, J. Cheng, J. Li, K. H. L. Zhang, *J. Mater. Chem. A* **2020**, *8*, 4407–4415.
[8] W. Yang, S. Zhang, Q. Chen, C. Zhang, Y. Wei, H. Jiang, Y. Lin, M. Zhao, Q. He, X. Wang, Y. Du, L. Song, S. Yang, A. Nie, X. Zou, Y. Gong, *Adv. Mater.* **2020**, *32*, 2001167.
[9] G. L. Chai, K. Qiu, M. Qiao, M. M. Titirici, C. Shang, Z. Guo, *Energy Environ. Sci.* **2017**, *10*, 1186–1195.
[10] Y. Yang, W. Zhang, Y. Xiao, Z. Shi, X. Cao, Y. Tang, Q. Gao, *Appl. Catal. B* **2019**, *242*, 132–139.
[11] X. Zhao, P. Pachfule, S. Li, J. Ron, J. Simke, J. Schmidt, A. Thomas, *Angew. Chem. Int. Ed.* **2018**, *57*, 8921–8926.
[12] H. Hu, Z. Wang, L. Cao, L. Zeng, C. Zhang, W. Lin, C. Wang, *Nat. Chem.* **2021**, *13*, 358–366.
[13] J. Greeley, T. F. Jaramillo, J. Bonde, I. Chorkendorff, J. K. Nørskov, *Nat. Mater.* **2006**, *5*, 909–913.
[14] J. Wang, T. Liao, Z. Wei, J. Sun, J. Guo, Z. Sun, *Small Methods* **2021**, *5*, 2000988.
[15] Y. Chen, X. Li, K. Park, J. Song, J. Hong, L. Zhou, Y. W. Mai, H. Huang, J. B. Goodenough, *J. Am. Chem. Soc.* **2013**, *135*, 16280–16283.
[16] Z. W. She, J. Kibsgaard, C. F. Dickens, I. Chorkendorff, J. K. Nørskov, T. F. Jaramillo, *Science* **2017**, *146*, 355.
[17] Y. Pan, K. Sun, S. Liu, X. Cao, K. Wu, W. C. Cheong, Z. Chen, Y. Wang, Y. Li, Y. Liu, D. Wang, Q. Peng, C. Chen, Y. Li, *J. Am. Chem. Soc.* **2018**, *140*, 2610–2618.
[18] H. Xue, A. Meng, H. Zhang, Y. Lin, Z. Li, C. Wang, *Nano Res.* **2021**, *14*, 4173–4181.
[19] Y. Pan, D. Heryadi, F. Zhou, L. Zhao, G. Lestari, H. Su, Z. Lai, *CrystEngComm* **2011**, *13*, 6937–6940.
[20] L. He, L. Li, L. Zhang, S. Xing, T. Wang, G. Li, X. Wu, Z. Su, C. Wang, *CrystEngComm* **2014**, *16*, 6534–6537.
[21] J. Zhao, X. Quan, S. Chen, Y. Liu, H. Yu, *ACS Appl. Mater. Interfaces* **2017**, *9*, 28685–28694.
[22] L. Ji, J. Wang, X. Teng, T. J. Meyer, Z. Chen, *ACS Catal.* **2020**, *10*, 412–419.
[23] X. Zhao, P. Pachfule, S. Li, J. R. J. Simke, J. Schmidt, A. Thomas, *Angew. Chem. Int. Ed.* **2018**, *57*, 8921–8926.
[24] Y. Li, M. Lu, Y. Wu, Q. Ji, H. Xu, J. Gao, G. Qian, Q. Zhang, *J. Mater. Chem. A* **2020**, *8*, 18215–18219.
[25] Z. Zhao, X. Zhou, K. Kou, H. Wu, *Carbon* **2021**, *173*, 80–90.
[26] W. Zhang, A. Arramel, P. K. J. Wong, L. Zhang, J. Zheng, W. Zhang, H. Zhang, X. Yan, J. Qi, J. Li, *J. Mater. Chem. A* **2020**, *8*, 14653–14660.
[27] Q. Lai, Y. Zhao, Y. Liang, J. He, J. Chen, *Adv. Funct. Mater.* **2016**, *26*, 8334–8344.
[28] C. Lin, S. S. Shinde, Z. Jiang, X. Song, Y. Sun, L. Guo, H. Zhang, J. Y. Jung, X. Li, J. H. Lee, *J. Mater. Chem. A* **2017**, *5*, 13994–14002.
[29] B. You, N. Jiang, M. Sheng, W. S. Drisdell, J. Yano, Y. Sun, *ACS Catal.* **2015**, *5*, 7068–7076.
[30] H. Jin, J. Wang, D. Su, Z. Wei, Z. Pang, Y. Wang, *J. Am. Chem. Soc.* **2015**, *137*, 2688–2694.
[31] Y. Pan, H. Ren, R. Chen, Y. Wu, D. Chu, *Chem. Eng. J.* **2020**, *398*, 125660.

[32] J. Gorimbo, R. Muvhiiwa, E. Llane, D. Hildebrandt, *Reactions* **2020**, *1*, 115–129.
[33] L. Bai, C. S. Hsu, D. T. L. Alexander, H. M. Chen, X. Hu, *J. Am. Chem. Soc.* **2019**, *141*, 14190–14199.
[34] Y. Li, S. Li, Y. Wang, J. Wang, H. Liu, X. Liu, L. Wang, X. Liu, W. Xue, N. Ma, *Phys. Chem. Chem. Phys.* **2017**, *19*, 11631–11638.
[35] J. Hao, W. Yang, Z. Zhang, J. Tang, *Nanoscale* **2015**, *7*, 11055–11062.
[36] C. J. Chang, S. C. Lin, H. C. Chen, J. Wang, K. J. Zheng, Y. Zhu, H. M. Chen, *J. Am. Chem. Soc.* **2020**, *142*, 12119–12132.
[37] L. Chen, Y. Zhang, H. Wang, Y. Wang, D. Li, C. Duan, *Nanoscale* **2018**, *10*, 21019–21024.
[38] X. Hu, G. Luo, X. Guo, Q. Zhao, R. Wang, G. Huang, B. Jiang, C. Xu, F. Pan, *Sci. Bull.* **2021**, *66*, 708–719.
[39] X. Cao, Y. Tan, H. Zheng, J. Hu, X. Chen, Z. Chen, *Phys. Chem. Chem. Phys.* **2022**, *24*, 4644–4652.
[40] B. Liu, B. Cao, Y. Cheng, P. Jing, J. Zhao, R. Gao, A. O'Mullane, H. Zhu, K. Liu, X. Sun, Y. Du, J. Zhang, *iScience* **2020**, *23*, 101264.
[41] K. Zhou, B. Mousavi, Z. Luo, S. Phatanasri, S. Chaemchuen, F. Verpoort, *J. Mater. Chem. A* **2017**, *5*, 952–957.
[42] J. Shi, F. Qiu, W. Yuan, M. Guo, Z. H. Lu, *Chem. Eng. J.* **2021**, *403*, 126312.
[43] L. Song, J. Chang, Y. Ma, X. Tan, Y. Xu, L. Guo, Z. Chen, T. Zhao, Y. Li, Y. Liu, Y. Zhang, W. Chu, *RSC Adv.* **2020**, *10*, 43248–43255.
[44] Q. Jin, B. Ren, H. Cui, C. Wang, *Appl. Catal. B* **2021**, *283*, 119643.
[45] H. Fei, J. Dong, Y. Feng, C. S. Allen, C. Wan, B. Volosskiy, M. Li, Z. Zhao, Y. Wang, H. Sun, P. An, W. Chen, Z. Guo, C. Lee, D. Chen, I. Shakir, M. Liu, T. Hu, Y. Li, A. I. Kirkland, X. Duan, Y. Huang, *Nat. Catal.* **2018**, *1*, 63–72.
[46] J. Xie, H. Zhang, S. Li, R. Wang, X. Sun, M. Zhou, J. Zhou, X. W. Lou, Y. Xie, *Adv. Mater.* **2013**, *25*, 5807–5813.
[47] M. P. Marceta Kaninski, V. M. Nikolic, G. S. Tasic, Z. L. Rakocevic, *Int. J. Hydrogen Energy* **2009**, *34*, 703–709.
[48] M. Bajdich, M. García-Mota, A. Vojvodic, J. K. Nørskov, A. T. Bell, *J. Am. Chem. Soc.* **2013**, *135*, 13521–13530.

Manuscript received: June 19, 2023
Revised manuscript received: July 18, 2023
Version of record online: August 7, 2023